UAV Fleet Charging on Telecom Towers with Differential Capacitive Wireless Power Transfer

Mian Liao, Student Member, IEEE, Tanuj Sen, Student Member, IEEE, Youssef Elasser, Member, IEEE, Hashim Al Hassan, Member, IEEE, Andrew Pigney, Member, IEEE, Edward Knapp, Senior Member, IEEE, and Minjie Chen, Senior Member, IEEE

Abstract—This paper introduces a capacitive differential wireless power transfer (DWPT) architecture to efficiently charge an array of unmanned aerial vehicles (UAVs) on a telecom tower as a UAV airport. A switched capacitor (SC) based ladder differential power processing (DPP) converter is utilized to regulate the voltages of multiple series-stacked wireless charging modules from a high-voltage DC bus. The half-bridge switches in the DPP circuit are reused as an inverter in a capacitive power transfer (CPT) system with a double-sided LC-compensation network, featuring reduced semiconductor component count and device stress. The capacitive coupling plates are integrated into landing platforms and UAV landing gears for high coupling capacitance and minimum influence on aerodynamics. An experimental prototype and related design considerations are presented to achieve high efficiency and ensure robust performance against misalignments. The DWPT architecture is verified through an 8port DPP converter supporting up to 8 CPT charging modules.

Index Terms—differential power processing, capacitive wireless power transfer, multi-port converter, wireless UAV charging

I. INTRODUCTION

Unmanned aerial vehicles (UAVs) are increasingly utilized across various industries due to their versatility and efficiency. They are promising to serve in agriculture for monitoring crop health, in logistics for delivering goods, in surveillance for enhancing security, and in environmental monitoring to track changes in ecosystems. However, one of the primary limitations hindering the broader deployment of UAVs is their restricted operational time, affected largely by battery capacity. As battery life limits the range and duration of flights, full automation of UAV systems requires frequent landing and recharging. Additionally, UAVs typically operate in fleets, requiring them to be charged simultaneously.

Wireless power transfer (WPT) is an attractive technology for charging UAVs because of its flexibility, safety features, and convenience. As illustrated in Fig. 1, it is attractive to place wireless UAV charging stations on telecom towers so

This paper is an extension of a previously published conference paper, "Drone Charging Stations on Telecom Towers with Series-Stacked Capacitive Differential Wireless Power Transfer" in IEEE APEC 2024 [1]. This work was supported by American Tower Corporation through the Princeton Andlinger Center E-ffiliates Program. (Corresponding Author: Minjie Chen)

M. Liao, T. Sen, Y. Elasser and M. Chen are with the Department of Electrical and Computer Engineering and the Andlinger Center for Energy and the Environment at Princeton University, Princeton, NJ, 08540, USA (email: mianl, tsen, yelasser, minjie@princeton.edu).

H. Al Hassan, A. Pigney and E. Knapp are with American Tower Corporation, Boston, MA, 02116, USA (e-mail: Hashim.Alhassan, Andrew.Pigney, Edward.Knapp@americantower.com).

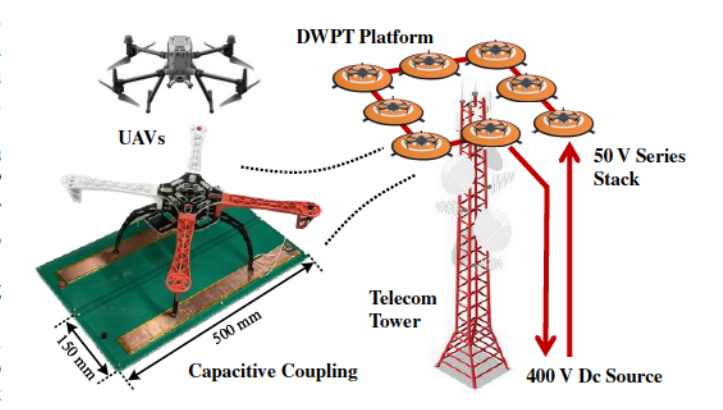


Fig. 1. Principles of the differential wireless power transfer platform with series-stacked UAV charging stations. Power is delivered from 400 V on the ground to eight series stacked 50 V charging stations on the top of the tower.

UAVs can autonomously land on wireless charging transmitters and start charging without physical connections or human interactions, thus facilitating continuous operations of UAVs and greatly extending the capabilities of UAVs in various applications. WPT can be implemented with either inductive coupling [2] or capacitive coupling [3]. Inductive power transfer (IPT) uses a magnetic field to transfer power, while capacitive power transfer (CPT) uses an electric field for power delivery [4], [5]. Compared to IPT, CPT has the advantage of eliminating the need for bulky magnetic components, reducing the weight of the UAVs, and allowing for larger payloads to be serviced. CPT receivers can also be integrated with UAV structures such as landing gears, and the coupling between the transmitter and the receiver is generally less susceptible to misalignment [6]. One can also combine IPT and CPT technologies to further improve the wireless power transfer capability [7].

Traditional multi-access UAV charging systems do not leverage the uniform charging profile of UAV fleets [8]–[10]. Differential power processing (DPP) is appealing when there is a single high-voltage power source available to power multiple devices with similar power needs [11], [12]. It features high efficiency and high-power density, which have been validated in various applications such as data center power supplies [13], photovoltaic converters [14]–[16], battery balancers [17]–[19], etc. DPP can inherently step down the input voltage, alleviating voltage stresses on series-stacked loads and enabling high voltage power delivery. Rather than dealing with

Fig. 2. An example multi-access wireless UAV charging system using a 400 V high voltage dc bus based on a grid-edge telecom tower ecosystem: (a) the traditional architecture charging each UAV independently; (b) the proposed hybrid-switched-capacitor DWPT solution, using DPP for efficient power distribution to each WPT module for UAV charging. The WPT modules and the DPP architecture are combined to reduce the component count and power conversion stress. This architecture allows power delivery at high voltage (400 V) in the telecom towers and reduces the weight of the power delivery cables.

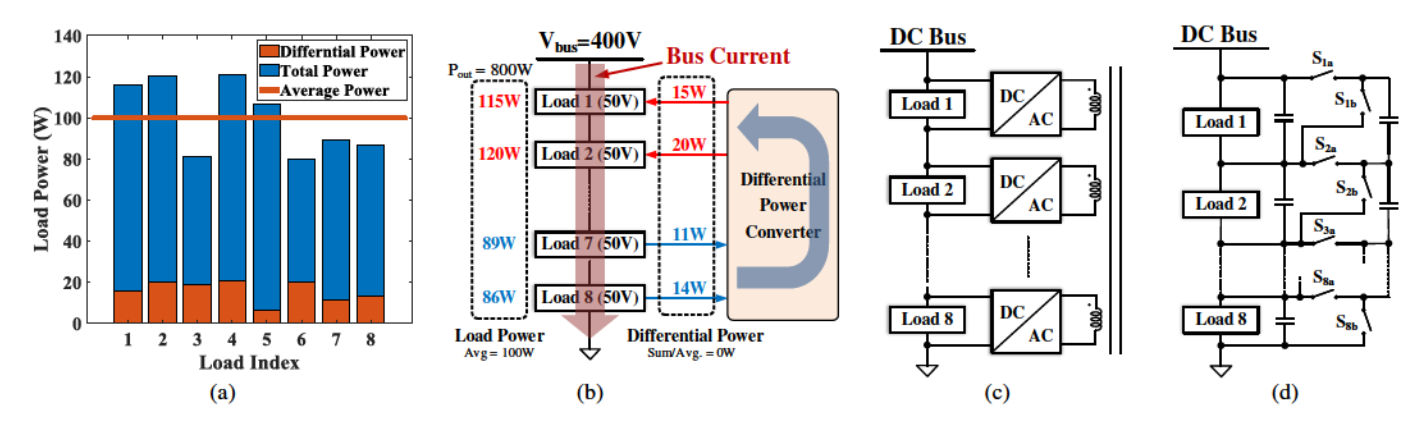


Fig. 3. (a) An example of the load power distribution for an 8-port DPP converter. The total output power is 800 W and the average load power is 100 W. Each load has less than 20% power variation from the average power. (b) The block diagram of an 8-port DPP converter demonstrates the power flow management. 400 V voltage bus is supplied as input and each load requires a 50 V dc voltage. (c) The DPP architecture based on a multi-winding transformer. (d) The DPP architecture based on ladder switched capacitors.

the full power rating of each load, DPP aims to equalize the differential power across loads, significantly minimizing losses. The system efficiency of a DPP converter is determined by the conditions of the loads [20].

Fig. 2 compares a conventional independent architecture and the proposed differential wireless power transfer (DWPT) architecture. The conventional solution utilizes several dcdc converters to reduce voltages from a 400 V high-voltage dc bus. DWPT architecture links a series of WPT modules, handling only the differential power among the modules.

This paper proposes a differential capacitive wireless power transfer method that integrates WPT modules and the switched-capacitor (SC) based ladder DPP converter to efficiently charge multiple UAVs on the top of the telecom tower. By combining and reusing the switches in both WPT modules and the DPP converter, it reduces the number of components, improves the power density, reduces the power loss, and enables power delivery at a higher voltage (400 V vs.

48 V). The capacitive wireless power couplers are embedded in both the landing platforms and the UAV landing gears to enhance coupling capacitance. A double-sided LC-compensation network is implemented to optimize system efficiency and improve tolerance to misalignment. The effects of misalignment is thoroughly analyzed and the practical design considerations of combining DPP and WPT are demonstrated. An 8-port DWPT UAV charging array is built and tested to validate the effectiveness of the proposed architecture and system design.

2

II. HYBRID SWITCHED-CAPACITOR WIRELESS POWER TRANSFER WITH DPP

A. Principles and Comparisons of DPP Converters

Various DPP solutions have been employed for different applications, especially for driving multiple loads with similar power levels [13], [17]. WPT for UAV charging is well-suited for DPP converters, as multiple UAVs, typically requiring similar charging power, are often charged simultaneously.

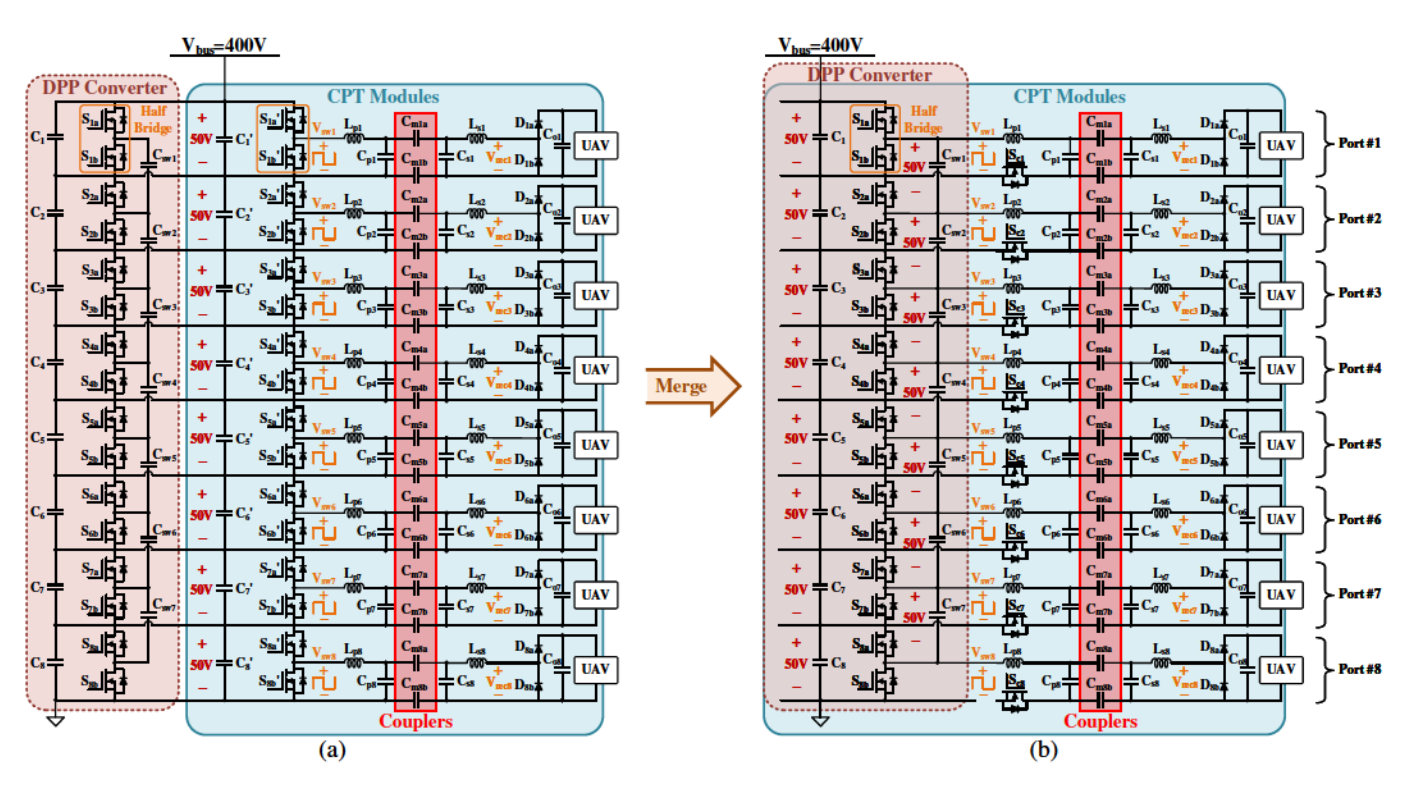


Fig. 4. (a) Standalone DWPT architecture with switches working independently for the DPP converter and the CPT modules. (b) Proposed integrated DWPT architecture merges the DPP converter and the CPT modules together in one system to drive an array of series-stacked CPT transmitters and receivers. Both inductive and capacitive wireless power transfer mechanisms are applicable.

Fig. 3 (a) illustrates an example of the load power distribution in an 8-port DPP converter. The blue bars represent the power requirement for each load, while the red bars represent the difference between each load's power and the average load power. In this example, the power required by each load differs from the average by less than 20%. Fig. 3 (b) demonstrates the power flow in this 8-port DPP converter, which operates with a 400 V bus voltage and delivers a total output power of 800 W. A bus current flows through all series-stacked loads, providing them with equal power. Loads requiring less power will redistribute the recess to those needing more through the DPP converter. Ultimately, the dc voltage across each load balances at 50 V, enabling the system to achieve inherent voltage stepdown from the high-voltage bus. In this scenario, the DPP converter only manages less than 20% of the total output power, significantly reducing power loss and device stress. Fig. 3 (c) and (d) depict two common DPP architectures: one utilizing a multi-winding transformer [13] and the other based on switched capacitors [21]. The transformer-based DPP converter offers benefits such as compact system design and port-to-port galvanic isolation. However, the magnetic flux and power coupling in a multi-winding transformer requires more sophisticated phase-shift control, adding to design complexity [22]. This paper specifically focuses on the SC-based ladder DPP, leveraging its low component count, compact size, and straightforward control. The operation principles of the SCladder DPP are also correlated to the multitrack architecture as presented in [23], [24], replacing the multi-winding transformer coupling with capacitive wireless coupling. The

SC-based ladder architecture also equalizes the voltage stress across all capacitors, ensuring that the dc voltages of the DPP output capacitors match those of the switched capacitors.

3

B. Design of a CPT System for UAV Charging

A typical CPT module shown in Fig. 4 (a) consists of a halfbridge inverter, LC compensators, capacitive couplers, and a half-bridge rectifier. In UAV applications, the small area of the coupling plate on the receiver end may lead to weak coupling, making capacitive coupling attractive [6]. To deliver high power despite the limited coupling capacitance, either high frequency or high voltage is necessary. The LC compensator acts as a voltage step-up matching network on the transmitter side and a voltage step-down transformer on the receiver side, aiming to increase the voltage across the capacitive coupler and thus enhance the power level. To achieve higher power and efficiency, multi-stage compensation networks such as LCLC or CLLC may be utilized at the expense of a more complicated circuit [25]. This paper uses a single-stage LC compensator as an example to demonstrate the effectiveness of the DWPT architecture. Additionally, the half-bridge circuit employed by the DPP converter can also serve as a half-bridge inverter that generates the high-frequency square wave fed into the compensation network. The half-bridge rectifier, together with the output capacitors, regulates the DC current supplied to the UAV. This structure is replicated across all eight CPT modules which are designated as Port #1 through Port #8.

Fig. 5. Working principles of an 8-port DWPT converter: (a) Phase 1 when the top side switches S_{1a} to S_{8a} turn on and high voltages are fed into CPT modules; (b) Phase 2 when the bottom side switches S_{1b} to S_{8b} turn on and 0 V is fed into CPT modules.

C. Proposed Integrated DWPT Architecture

The DPP converter and multiple WPT modules can be combined as a DWPT architecture to deliver low-voltage UAV charging power from a high-voltage bus. The standalone DWPT architecture shown in Fig. 4 (a) has two sets of switches working independently for the DPP converter and the CPT modules, making the system bulky and lossy. The proposed DWPT architecture enables combined usage of the switches for DPP and WPT, leading to a significantly reduced component count. Fig. 4 (b) demonstrates the integration of the DPP switches with the CPT switches. Notably, the proposed DWPT architecture is versatile and can be applied to both IPT and CPT structures, with this paper emphasizing CPT as an illustrative example.

The DPP converter shown in Fig. 4 (b) consists of eight series-stacked DPP output capacitors C_1-C_8 , seven switched capacitors $C_{sw1}-C_{sw7}$, and sixteen series-stacked switches $S_{1a}-S_{8b}$, with "a" and "b" referring to the top and bottom switch of each half-bridge unit. The output capacitors of the DPP converter are reused as the input capacitors of the CPT modules. Fig. 5 presents the DPP working principle for voltage balancing at the input of each CPT module. In phase 1, when the top switches $S_{1a}-S_{8a}$ of half-bridge circuits turn on as depicted in Fig. 5 (a), the switched capacitor $C_{sw1}-C_{sw7}$ is connected in parallel with the capacitor C_1-C_7 . As a result, the capacitors C_n and C_{swn} jointly provide the input

voltage V_{swn} to the CPT module. In phase 2, when the bottom switches $S_{1b} - S_{8b}$ of half-bridge circuits turn on as shown in Fig. 5 (b), the switched capacitor $C_{sw1} - C_{sw7}$ is connected in parallel with the capacitor $C_2 - C_8$. Therefore, the input port of the CPT module is shorted in this case, resulting in zero applied voltage. The half-bridge circuit functions as the inverter, generating a square wave for the CPT module by periodically switching between phases 1 and 2 with equal time duration. The switched capacitor C_{swn} serves as an energy buffer, transferring charge between the two nearest capacitors C_n and C_{n+1} and maintaining voltage balance for all DPP output capacitors. Differential power is transferred between two adjacent ports, resulting in the intrinsic balancing of voltages. When the transmitter is not loaded, the power consumption of the unloaded port is very low. The DPP converter redistributes excess power from unloaded ports to the other connected with UAVs, ensuring that high input voltage is evenly distributed across the circuit. This allows for a balanced and lower dc voltage at each individual port. The voltage stresses of the DPP output capacitors and switched capacitors are constantly kept at 50 V.

Cut-off switches $S_{c1} \sim S_{c8}$ shown in Fig. 4 (b) are added in series with CPT modules to mitigate large circulating currents when the UAVs are not connected to the ports. This addition is necessary because all half-bridge inverters require continuous operation to maintain voltage balance in the DPP converter. Consequently, square waves are continuously supplied to the CPT modules, even in the absence of UAVS, resulting in excessive power loss through the LC compensation networks. This issue can be addressed by turning the cut-off switches on when UAVs are present, and turning them off when UAVs are not connected or fully charged. Although the LC compensation network necessitates cut-off switches, higher-order compensation networks may solve the issue of circulating currents by exhibiting high impedance at no-load conditions.

III. CAPACITIVE WIRELESS POWER TRANSFER FOR UAVS

Fig. 6 (a) shows a single CPT module with the capacitive coupler, represented by two series-connected mutual capacitors C_{m1} and C_{m2} , and two parallel self-capacitors C_{in1} and C_{in2} . Two external capacitors C_{ex1} and C_{ex2} are connected in parallel with C_{in1} and C_{in2} to increase the equivalent self-capacitance and resonate with the series inductors L_p and L_s to create the high voltage. Fig. 6 (b) illustrates the design of the capacitive coupler. The transmitter side has two terminals T_1 and T_2 that are designed as the two metal landing platform plates covered with the insulator. The receiver side has two terminals R_1 and R_2 integrated into two landing gears of the UAV.

A. Characteristics of the CPT System

Fig. 7 (a) shows a simplified CPT circuit model modified from Fig. 6 (a). The method of fundamental harmonics approximation (FHA) is used to replace the input square wave with a pure sinusoidal wave and the output half-bridge rectifier with

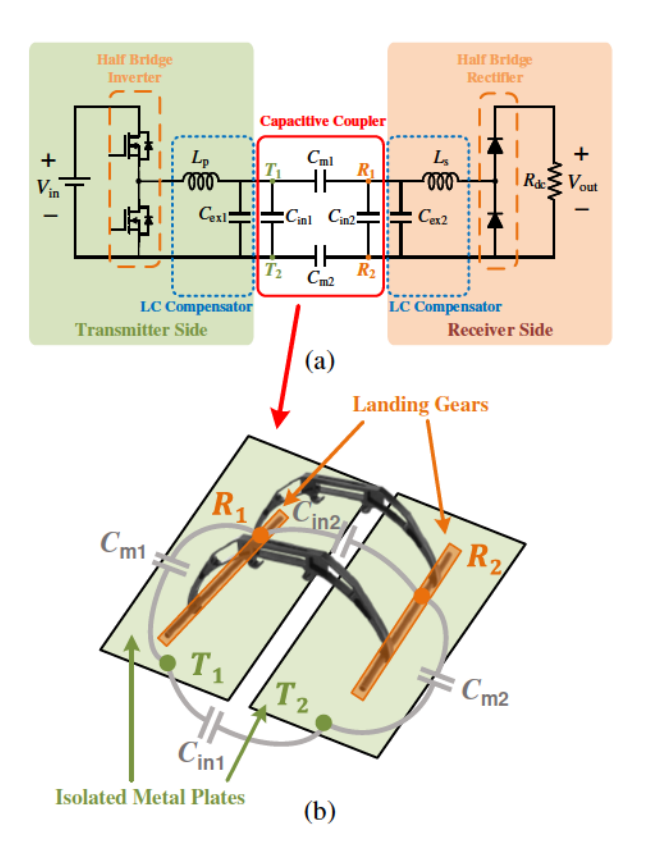


Fig. 6. (a) The schematic of the designed CPT system with a half-bridge inverter, half-bridge rectifier, capacitive coupler, and a double-sided LC compensator. (b) Capacitive coupler design based on metal plates and the landing gears of the UAV.

an equivalent resistor, resulting in equivalent ac output resistance $R_L = R_{dc} \times 2/\pi^2$. The equivalent ac rms input voltage is $V_{in1} = V_{in} \times \sqrt{2}/\pi$. The equivalent coupling capacitance is $C_m = C_{m1}C_{m2}/(C_{m1}+C_{m2})$. The equivalent self-capacitance on the transmitter side can be expressed as $C_p = C_{ex1} + C_{in1}$, while the equivalent self-capacitance on the receiver side is $C_s = C_{ex2} + C_{in2}$. In UAV applications, the weak crosscoupling between landing platforms and landing gears results in relatively smaller C_{in1} and C_{in2} compared to C_{ex1} and C_{ex2} . Hence, it is reasonable to assume that $C_p \approx C_{ex1}$ and $C_s \approx C_{ex2}$. V_p and V_s represent the voltages across selfcapacitance C_p and C_s . V_{m1} and V_{m2} represent the voltage across the coupling capacitance C_{m1} and C_{m2} . I_{in1} and I_{out1} represent the currents flowing into and out of the compensation network. They also denote the currents flowing through compensation inductors L_p and L_s . Fig. 7 (b) shows the behavioral circuit model where the capacitive coupling is represented by two voltage-controlled current sources. The self-capacitances are expressed as $C_1 = C_p + C_m$ and $C_2 = C_s + C_m$, while the coupling coefficient is defined as $k_c = C_m/\sqrt{C_1C_2}$. If the compensation network is symmetrically designed, the selfresonant frequency is $\omega_0 = 1/\sqrt{L_p C_1} = 1/\sqrt{L_s C_2}$.

To analyze the output voltage and current, the KCL equa-

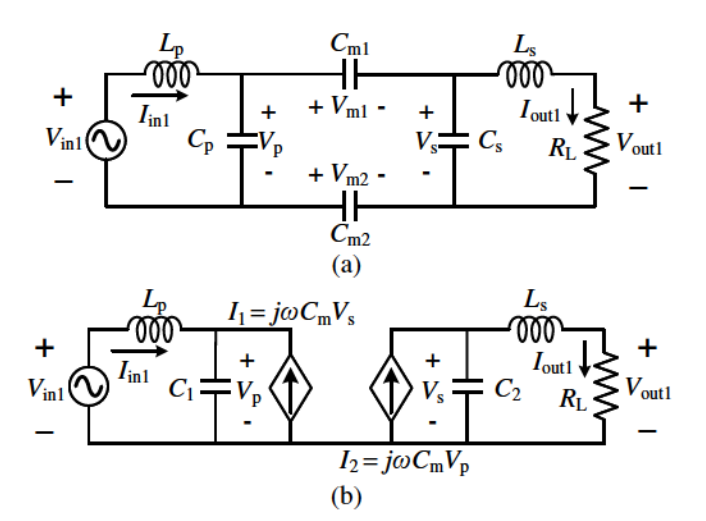


Fig. 7. (a) Simplified circuit model of the system. (b) Circuit behavioral model of the system.

tions are obtained with the admittances of the components [5]:

$$\begin{cases} Y_{Lp} \cdot (V_{in1} - V_p) + Y_m \cdot V_s = V_p \cdot Y_{C1} \\ Y_{Ls} \cdot (V_{out1} - V_s) + Y_m \cdot V_p = V_s \cdot Y_{C2} \\ Y_{Ls} \cdot (V_s - V_{out1}) = V_{out} \cdot Y_{RL} \end{cases} \tag{1}$$

where $Y_m, Y_{Lp}, Y_{Ls}, Y_{C1}, Y_{C2}$ and Y_{RL} denote the admittance of C_m, L_p, L_s, C_1, C_2 and R_L , respectively.

The voltage gain $G_v = V_{out1}/V_{in1}$ can be expressed as:

$$G_v = \frac{Y_{Lp} Y_{Ls} Y_m}{(Y_1 Y_2 - Y_m^2) Y_{RL} + (Y_1 Y_{C2} - Y_m^2) Y_{Ls}}$$
(2)

where $Y_1 = Y_{Lp} + Y_{C1}$ and $Y_2 = Y_{Ls} + Y_{C2}$. When the voltage gain is independent of the load Y_{RL} , the output can be constant voltage (CV). The magnitude of the voltage gain and the frequency in CV mode are:

$$\begin{cases} |G_v| = \sqrt{\frac{C_1}{C_2}} \\ \omega_{cv1} = \frac{1}{\sqrt{1+k_c}} \cdot \omega_0 \\ \omega_{cv2} = \frac{1}{\sqrt{1-k_c}} \cdot \omega_0 \end{cases}$$
 (3)

The transconductance $G_i = I_{out1}/V_{in1}$ can be expressed as:

$$G_i = \frac{Y_{Lp}Y_{Ls}Y_m}{(Y_1Y_2 - Y_m^2) + (Y_1Y_{C2} - Y_m^2)Y_{Ls}R_L}.$$
 (4)

When the transconductance is independent of the load R_L , the output can be constant current (CC). The magnitude of the transconductance and the frequency in CC mode are:

$$\begin{cases} |G_i| = \frac{\omega_{cc}C_m(1-k_c^2)}{k_c^2} \\ \omega_{cc} = \frac{1}{\sqrt{1-k_c^2}} \cdot \omega_0 \end{cases}$$
 (5)

TABLE I PARAMETER DESIGN

Parameter	Value	Parameter	Value
V_{in}	400 V	V_{out}	50 V
f_{sw}	1.5 MHz	k_c	18.2%
L_p	$5.0~\mu\mathrm{H}$	L_s	5.0 μH
C_p	2250 pF	C_s	2250 pF
C_{m1}	1000 pF	C_{m2}	1000 pF

B. Parameter Design

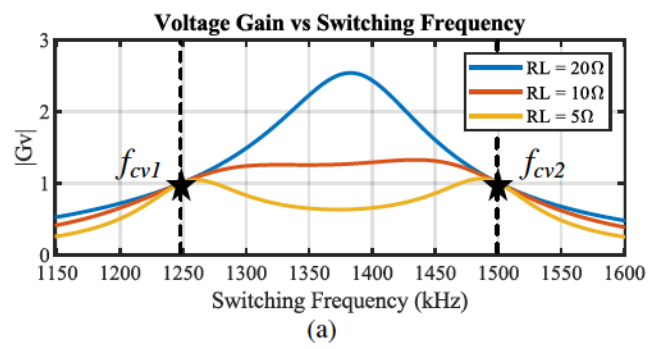
When a UAV lands on the platform, the landing gears and the landing platform are close to each other, thus the system can achieve a significantly greater coupling capacitance compared to other CPT applications such as Electric Vehicle (EV) wireless charging [5]. For a similar resonant frequency and coupling coefficient, this enhanced coupling capacitance allows for a compensation network design with larger capacitance in parallel and reduced inductance in series. For typical CPT applications, the capacitance is in the nF range and the inductance is in the μ H range. The size and weight of the system are mostly affected by the inductor. Therefore, reducing the inductance can help to mitigate the additional size and weight of the UAV, thus maintaining the aerodynamic performance of the UAV.

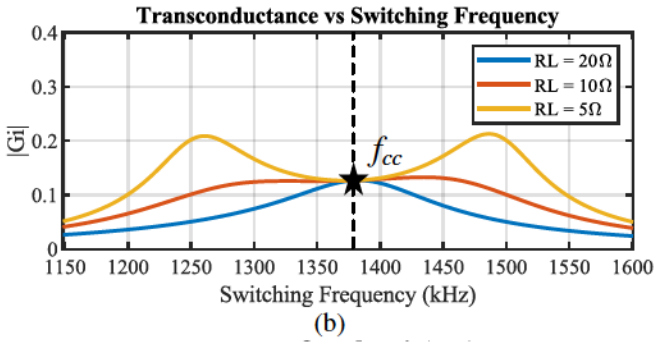
The SC-based DPP converter necessitates a consistent switching frequency across all half-bridge circuits, making individual frequency modulation impractical for each CPT module. The potential misalignment or foreign objects between the capacitive couplers can greatly impact the coupling capacitance. If the selected resonant frequency is correlated to the coupling capacitance, any deviation of resonant frequency due to misalignment or foreign objects may decrease output power and system efficiency. To address this challenge, the ideal switching frequency should be the resonant frequency of the LC compensation network, excluding the coupling capacitors. This frequency can be expressed as:

$$\omega_{sw} = \frac{1}{\sqrt{L_p C_p}} = \frac{1}{\sqrt{L_p (C_1 - C_m)}} \\
= \frac{1}{\sqrt{1 - \frac{C_m}{C_1}}} \frac{1}{\sqrt{L_p C_1}} \\
= \frac{1}{\sqrt{1 - k_c}} \cdot \omega_0 = \omega_{cv2}$$
(6)

The selected switching frequency is the same as the higher resonant frequency ω_{cv2} for the CV operational mode. The switching frequency is fixed across all operating conditions, and the system operates in an open loop. Additional battery management modules may be required between the DWPT converter and the batteries of UAVs to regulate the charging power.

To keep the CPT system symmetric and have a unity gain, the component values of the compensation networks are selected the same for both the transmitter side and the receiver side, which yield $L_1 = L_2$ and $C_p = C_s$. All





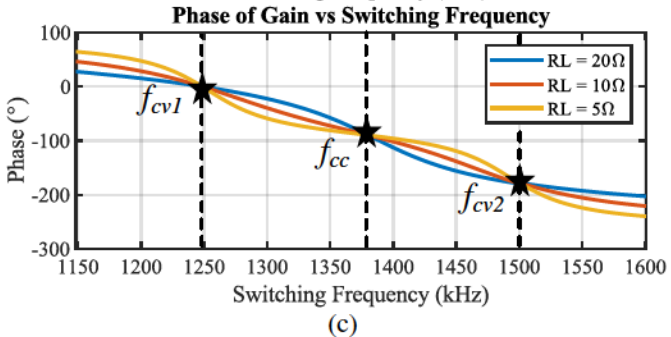


Fig. 8. Frequency and load characteristics of the designed CPT system with a double-sided LC compensation network. (a) Magnitude of voltage gain G_v . Two types of CV mode frequency are shown here. (b) Magnitude of transconductance G_i . One type of CC mode frequency is shown here. (c) Phase of G_v and G_i with 0° for f_{cv1} , -90° for f_{cc} and -180° for f_{cv2} .

the designed parameter values are shown in Table I. The individual capacitance between each plate and each landing gear is 1000 pF, resulting in an equivalent 500 pF coupling capacitance C_m . The coupling coefficient k_c is designed as 18.2%, striking a balance between CPT efficiency and system volume. Fig. 8 shows the frequency characteristics of the designed CPT system under different load conditions. Fig. 8 (a) displays the magnitude of voltage gain G_v as a function of the switching frequency, showcasing two types of CV mode frequency: $f_{cv1} = \omega_{cv1}/2\pi = 1.25$ MHz and $f_{cv2} = \omega_{cv2}/2\pi = 1.5$ MHz. The latter frequency f_{cv2} is selected as the switching frequency of the system to minimize the impact of fluctuating coupling capacitance. Fig. 8 (b) shows the magnitude of transconductance G_i , featuring one type of CC mode frequency at $f_{cc} = \omega_{cc}/2\pi = 1.38$ MHz. Fig. 8 (c) shows the phase angle of both G_v and G_i with 0° at f_{cv1} , -90° at f_{cc} , and -180° at f_{cv2} .

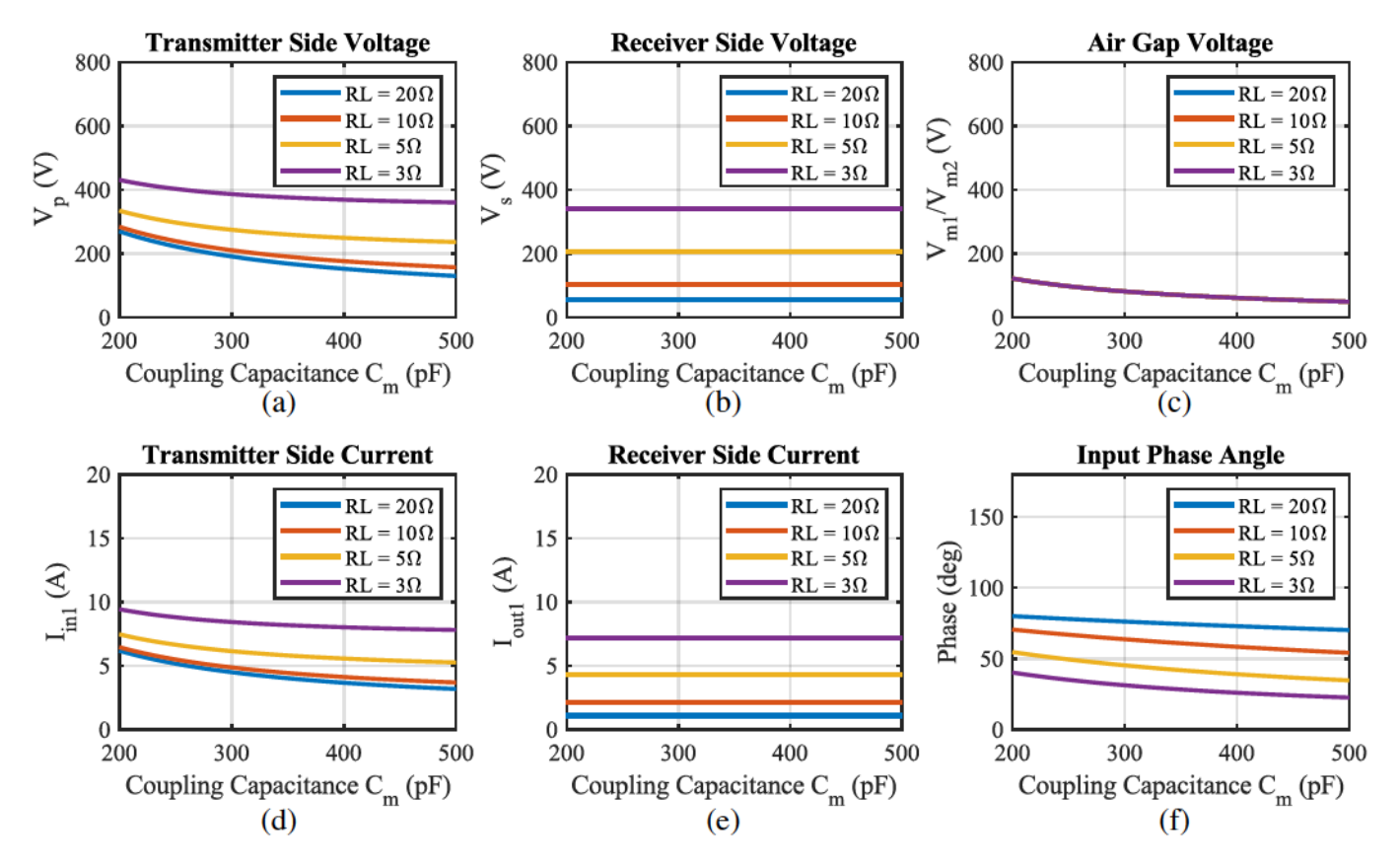


Fig. 9. Effects of misalignment on the characteristics of the system: a) Voltage of the compensation capacitor on the transmitter side; b) Voltage of the compensation capacitor on the receiver side; c) Voltage between two capacitive couplers; d) Current flowing through the compensation inductor on the transmitter side; e) Current flowing through the compensation inductor on the receiver side; f) Phase angle between the input voltage and current.

C. Analysis of Misalignment Tolerances

Misalignment of couplers in a CPT system can lead to reduced output power, decreased system efficiency, over-voltage risks, and potential device failure. Although the output voltage is less susceptible to the misalignment under the selected resonant frequency, understanding the impact of misalignment is crucial for maintaining the safe and efficient operation of the system. Misalignment typically occurs in two scenarios: 1) horizontal misalignment, where the UAV does not land precisely on the designated spot of the landing platform, reducing the coupling area; 2) vertical misalignment, caused by foreign objects between the landing platform and the UAV's landing gear, increasing the distance between the couplers. Both scenarios result in a coupling capacitance lower than the intended design value.

The variation of coupling capacitance leads to changes in the voltages and current across the compensation networks. The analysis below is based on the designed parameters and selected switching frequency $f_{cv2}=1.5\,$ MHz, where the output voltage is not affected by the coupling capacitance and the load resistance. From the equivalent circuit model shown in Fig. 7 (b), the receiver side capacitor voltage V_s can be expressed in terms of V_{out1} as:

$$V_s = V_{out1} (1 + \frac{1}{Y_{Ls} R_L}) \tag{7}$$

where the voltage is affected by the load resistance and is irrelevant to the coupling capacitance.

The transmitter side capacitor voltage V_p can be expressed in terms of V_{out1} as:

$$V_p = V_{out1} \frac{Y_{Ls}(Y_2 - Y_{Lp} + Y_2 Y_{RL})}{Y_m Y_{Ls}}$$
 (8)

where the voltage is affected both by the load resistance and the coupling capacitance.

For the symmetrical design, the couplers' air gap voltages $V_{m1} = V_{m2}$. They can be expressed in terms of V_{out1} as:

$$V_{m1} = V_{out1} \frac{Y_{Ls}(Y_2 - Y_{Lp} - Y_m) + Y_{RL}(Y_2 - Y_m)}{2Y_m Y_{Ls}}$$
(9)

with the switching frequency f_{cv2} , Y_2 is equal to Y_m and the equation can be further simplified as:

$$V_{m1} = V_{m2} = -V_{out1} \frac{Y_{Lp}}{2Y_m} \tag{10}$$

where the voltage is affected by the coupling capacitance and is irrelevant to the load resistance.

The transmitter side inductor current I_{in1} , the receiver side inductor current I_{out1} , and the input phase angle θ_{in} can be expressed as:

$$\begin{cases} I_{in1} = (V_{in1} - V_p) \cdot Y_{Lp} \\ I_{out1} = V_{out1} \cdot Y_{RL} \\ \theta_{in} = \angle V_{in1} - \angle I_{in1} \end{cases}$$
(11)

Fig. 9 illustrates the impact of varying coupling capacitance C_m due to misalignment in the CPT system, using the designed parameters and switching frequency. Fig. 9 (a) shows the voltage V_p of the compensation capacitor on the transmitter side, which increases as coupling capacitance decreases and load power increases. Fig. 9 (b) presents the voltage V_s of the compensation capacitor on the receiver side, which rises with increasing load power but remains unaffected by changes in coupling capacitance. Fig. 9 (c) depicts the voltage V_{m1}/V_{m2} between the capacitive couplers which increases as coupling capacitance decreases but is independent of load power. Fig. 9 (d) shows the current I_{in1} flowing through the compensation inductor on the transmitter side, which rises as both coupling capacitance decreases and load power increases. Fig. 9 (e) presents the current I_{out1} flowing through the compensation inductor on the receiver side, which increases with load power but is unaffected by changes in coupling capacitance. Fig. 9 (f) shows the input phase angle of the system, which increases with both reduced coupling capacitance and higher load power.

From this analysis, it is clear that the misalignment primarily affects the transmitter side and the capacitive couplers. The increased air gap voltage between the couplers generates a stronger electric field distribution, necessitating additional safety precautions. The higher voltage across the transmitter side's compensation capacitor results in increased voltage stresses on external capacitors. Additionally, the rise in inductor current on the transmitter side increases power losses in both the inductor and switches, which can ultimately lead to device failure. Despite the effects on the transmitter side, the receiver side remains unaffected by misalignment. This is advantageous for UAV applications, as UAVs are sensitive to the weight and size of receiver components. Therefore, no additional design considerations are necessary for the UAV side to mitigate misalignment issues.

IV. ANALYSIS AND DESIGN FOR NO-LOAD CONDITIONS

The SC-based DPP converter requires the continuous operation of all switches. Thus, high-frequency square waves are always fed into all the CPT modules. However, this can potentially lead to unintended circulating currents and excessive power loss when certain modules are not actively supplying power to the loads. The system typically encounters two distinct no-load conditions: 1) when the landing platform has no UAV present, causing the absence of the receiver side in the CPT module; 2) when a UAV is sitting on the landing platform but is fully charged, incapable of drawing any additional power. Both of these conditions need to be effectively addressed to reduce power loss and enhance the overall system efficiency.

A. No-Load Condition 1: UAV is not present

Fig. 10 (a) demonstrates what occurs when no UAV is docked on the charging platform, leading to the disconnection of the UAV's receiver side circuit. Additionally, the coupling capacitors are not engaged due to the absence of the coupling between the landing gear and the landing platform. In this configuration, only the transmitter side's compensation

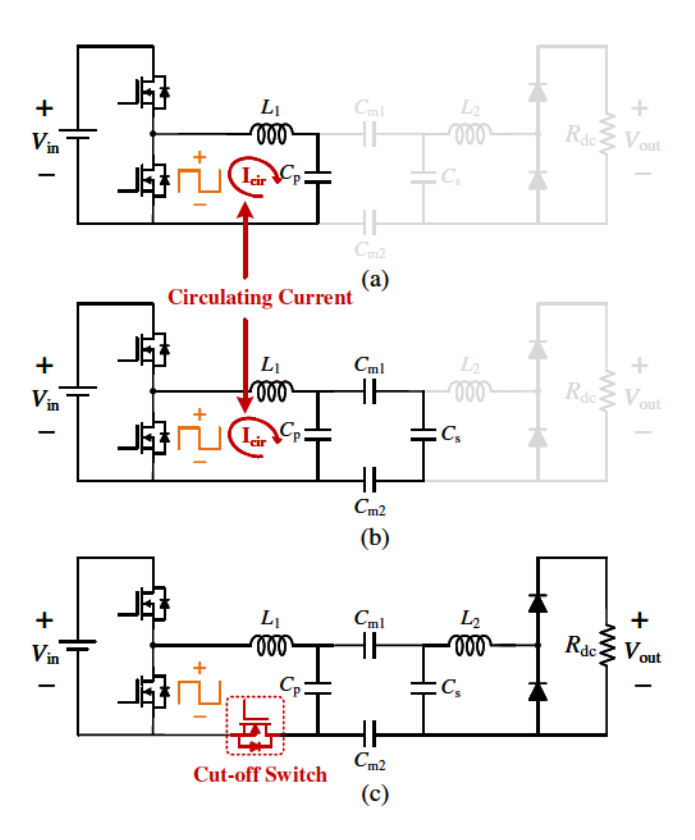


Fig. 10. (a) Equivalent circuit model under no-load condition 1 when UAV is not present. (b) Equivalent circuit model under no-load condition 2 when a UAV is present but not actively charged. (c) Proposed CPT circuit with a cut-off switch to mitigate circulating currents.

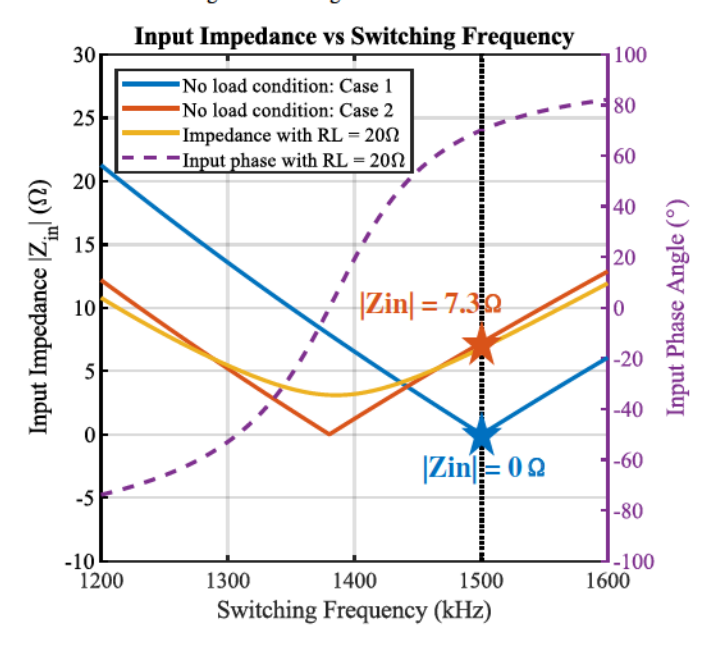


Fig. 11. Magnitude of input impedance and input phase angle with different switching frequency under no-load condition 1, no-load condition 2 and 5Ω output AC resistance R_L .

inductor L_1 and capacitor C_p remain connected in series with the input. If the compensation networks are symmetrically designed, the resonant frequency ω_{n1} in this condition aligns with the selected switching frequency, calculated in Equ. 6. It is expressed as:

$$\omega_{n1} = \omega_{sw} = \omega_{cv2} \tag{12}$$

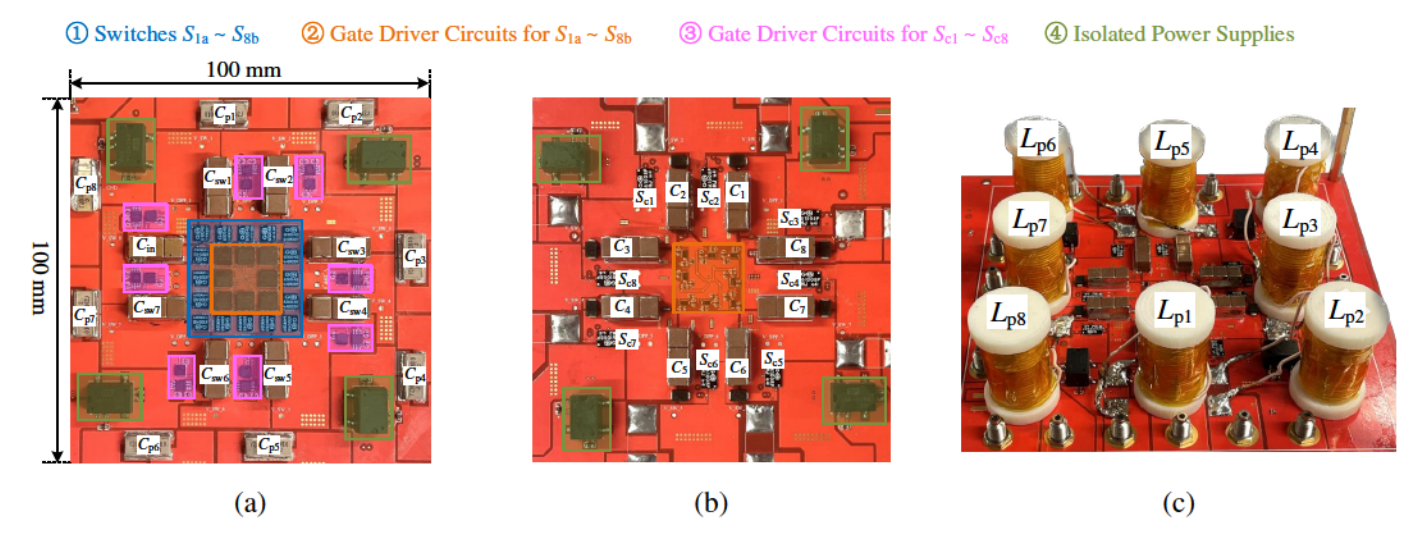


Fig. 12. The prototype of the main power board includes the DPP converter and the transmitter side of the CPT modules: (a) top side view; (b) bottom side view without inductors; (c) bottom side view with inductors.

The resonant frequency of no-load condition 1 is the same as the higher resonant frequency for the CV operational mode.

The input impedance of a CPT module is defined as:

$$Z_{in} = \frac{V_{in1}}{I_{in1}} \tag{13}$$

The blue curve in Fig. 11 shows the input impedance under no-load condition 1. Notably, the zero input impedance and short circuit occur at 1.5 MHz switching frequency, potentially leading to a substantial circulating current that could damage the circuit.

B. No-Load Condition 2: UAV is present but not charging

Fig. 10 (b) depicts the case when a UAV is positioned on the charging platform but is not actively charged. Under this circumstance, the load does not draw any current from the CPT module and the compensation inductor L_2 is detached from the circuit. However, a circulating current continues to flow through the remaining circuit components. The resonant frequency ω_{n2} for this specific condition is calculated as:

$$\omega_{n2} = \frac{1}{\sqrt{L_p(C_p + C_{m1}//C_s//C_{m2})}}$$

$$= \frac{1}{\sqrt{L_p(C_1 - C_m) + \frac{(C_2 - C_m)C_m}{C_2}}}$$

$$= \frac{1}{\sqrt{\frac{C_1C_2 - C_m^2}{C_1C_2}}} \frac{1}{\sqrt{L_pC_1}}$$

$$= \frac{1}{\sqrt{1 - k_c^2}} \cdot \omega_0 = \omega_{cc}$$
(14)

The resonant frequency of no-load condition 2 is the same as the resonant frequency for the CC operational mode.

The red curve in Fig. 11 shows the input impedance under no-load condition 2. Although the short circuit hazard does not appear here, the magnitude of input impedance remains low at 1.5 MHz switching frequency, resulting in excess circulating currents and large power loss. Therefore, it is necessary to

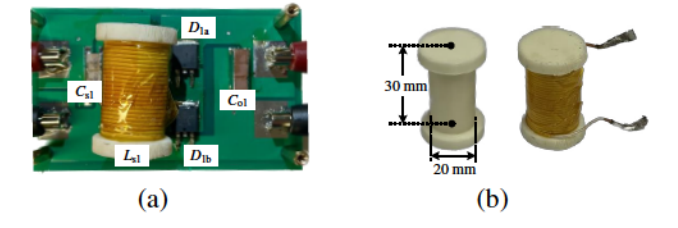


Fig. 13. The prototype of the receiver board includes a LC compensation network and a half-bridge rectifier: (a) top side view; (b) air core inductor.

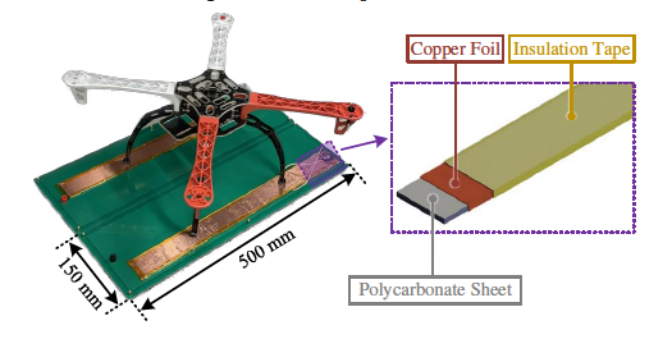


Fig. 14. Prototype of the capacitive coupler design. The transmitter plate consists of a PCB with a single copper layer serving as the conductor and a layer of solder mask acting as the insulator. The receiver plate is adapted from the UAV landing gear and features a polycarbonate frame encased in a single layer of conducting copper foil for conduction and a single layer of Kapton ® tape for insulation.

implement strategies to mitigate these circulating currents and enhance system efficiency across all conditions.

C. Addition of Cut-off Switch

The presence of the circulating current in no-load conditions 1 and 2 leads to significant power loss and potential short circuit risks. To address this problem, a cut-off switch is included in the returning path of each CPT module as shown in Fig. 10 (c). When the battery needs to be charged and power needs to be extracted from the CPT system, the cut-off switches are switched on. When no load condition 1 or 2 occurs, the cut-off switch are switched off and the transmitter side exhibits

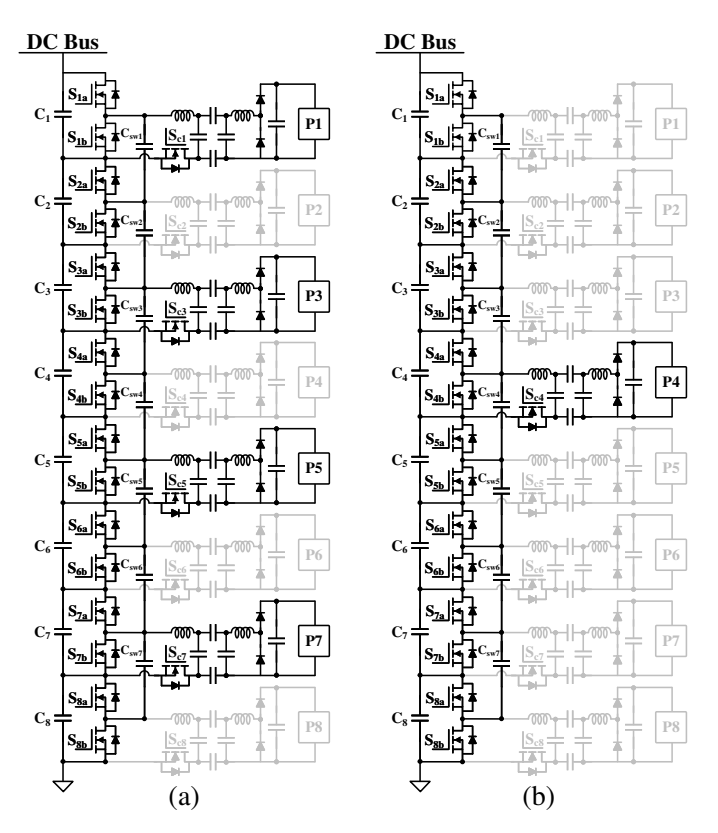


Fig. 15. Examples of load configurations: (a) Port #1, #3, #5 and #7 are connected with UAVs in an interleaved DPP operation; (b) Only Port #4 is connected with UAV, while all other ports remain inactive.

high impedance at the switching frequency, preventing any circulating currents and associated losses in the system. A switch with low turn-on resistance and relatively small drain-source capacitance is desirable for the cut-off switch.

V. EXPERIMENTAL VERIFICATION

A. Experimental Setup

An eight-port DWPT converter is designed and tested to step down the voltage from 400 V to 50 V. The wireless charger output voltage is also 50 V. The entire system is a combination of three parts: a main power board, multiple receiver boards, and arrays of capacitive couplers. The main power board, shown in Fig. 12, contains eight series-stacked half-bridge circuits which form the backbone of the DPP converter. Each of these half-bridge circuits is linked to one of the eight CPT modules by means of a cut-off switch, an LC compensation network, and a DPP output capacitor. In addition, there are seven switched capacitors, which together with the series-stacked half-bridge circuits function as the SC-DPP, facilitating voltage balancing. These half-bridge circuits simultaneously function as the inverters for the CPT modules. GaN Systems 100 V, 38 A (GS61004Bs) GaN switches are utilized as the switching devices, operating at 1.5 MHz with a fixed 50% duty ratio. All half-bridge circuits are controlled by one pair of complementary pulse-width-modulation (PWM) signals with 50% duty ratio and the system operates in an open loop. An isolated power supply (ISE0505A) along with

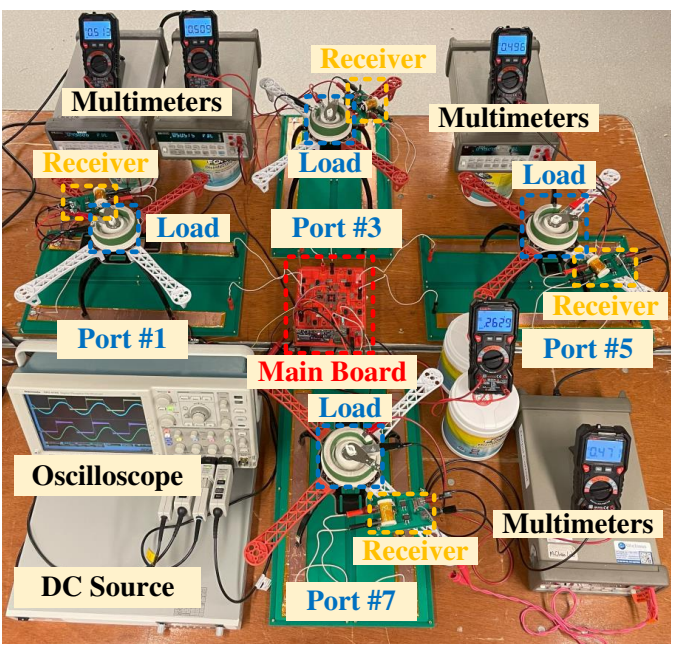


Fig. 16. Experimental setup for four ports operation, including a main board connected to landing platforms, four capacitive couplers built from landing gears and platforms, four receiver boards on top of UAVs, four adjustable resistors as loads, and a high-voltage DC power source.

an isolated half-bridge gate driver (2EDF7275K) is used in the gate driver circuitry to drive the half-bridge switches with series-stacked floating grounds. GaN Systems 100 V, 90 A (GS61008Ps) GaN switches are utilized as the cut-off switches for all CPT modules, which are turned on when an output port is loaded, and turned off at no load conditions to prevent circulating currents. A Digital Isolator IL711 and a low-side gate driver LM5114 are used to drive each of these cut-off switches. The cut-off switch is placed to share the same floating ground as the bottom switch in the half-bridge circuit, reducing the complexity of the gate driver circuit. The DPP output capacitors and the switched capacitors are both 132 μ F. The component values of the compensation network are selected the same as in Table I with a 2250 pF capacitance and a 5 μ H inductance on the transmitter side. Fig. 12 (a) shows the top side view of the main board including the halfbridge circuits, the switched capacitors and the transmitter side capacitors. In Fig. 12 (b), the bottom side view of the main board is presented which includes the cut-off switches and the DPP output capacitors. The placement of the transmitter side inductors on the bottom side of the main power board is shown in Fig. 12 (c). Eight CPT modules are symmetrically distributed around the center, with two on each side of the rectangular board.

The receiver board, shown in Fig. 13 (a) holds the rectifier diodes, output capacitors, receiver side capacitors and inductors. Vishay VB20100S-E3 is utilized as the rectifier diode for efficient rectification. The output capacitors are 132 μ F. The receiver side LC compensator has a 2250 pF capacitance and a 5 μ H inductance, which are the same as the transmitter side, resulting in a symmetric CPT system. Fig. 13 (b) shows the

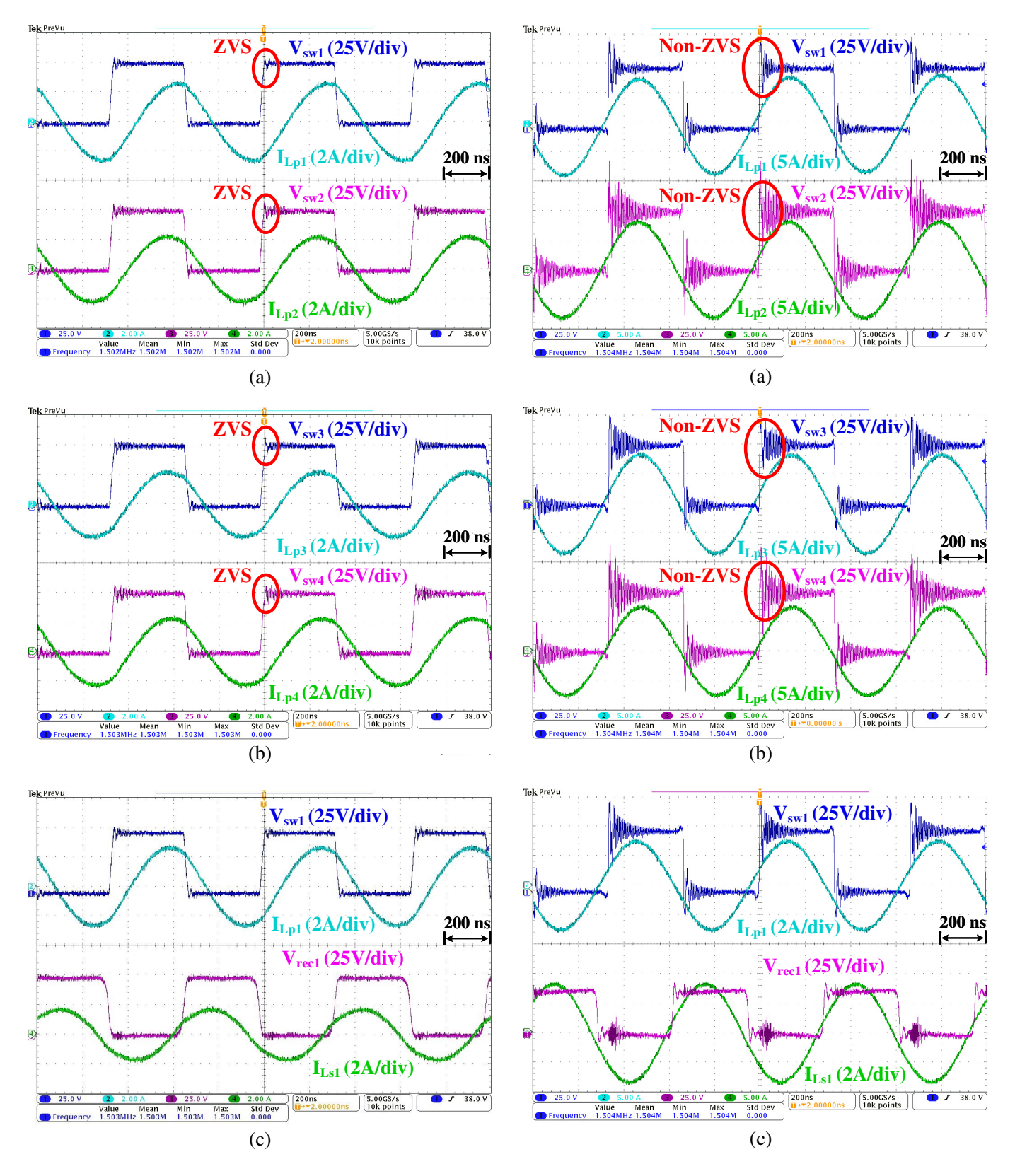


Fig. 17. Waveforms of Port #1, #2, #3 and #4 under 400 V input voltage, scenario (2), 100 W total output power, and 1.5 MHz switching frequency: (a) input voltages and current of Port #1 and Port #2; (b) input voltages and current of Port #3 and Port #4; (c) input and output switched-node voltages and currents of Port #1. Soft switching is achieved at all ports.

Fig. 18. Waveforms of Port #1, #2, #3 and #4 under 400 V input voltage, scenario (2), 400 W total output power, and 1.5 MHz switching frequency: (a) input voltages and current of Port #1 and Port #2; (b) input voltages and current of Port #3 and Port #4; (c) input and output switched-node voltages and currents of Port #1. A few ports lost soft switching.

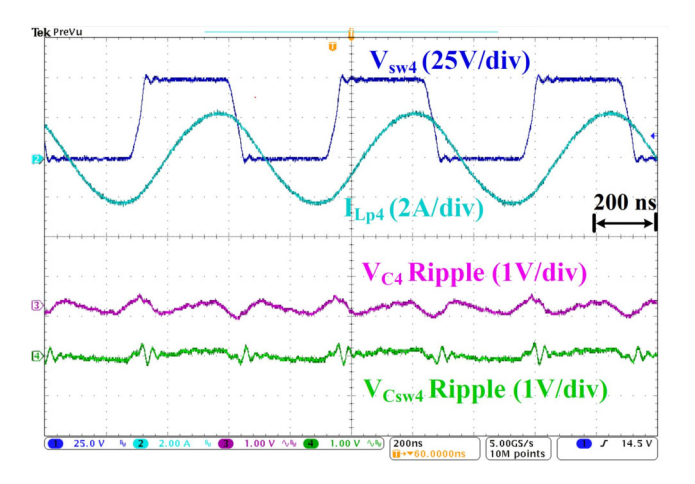


Fig. 19. Waveform under 400 V input voltage, scenario (3), 25 W output power, and 1.5 MHz switching frequency. The switched node voltage V_{sw4} and input current I_{Lp4} of Port #4 are shown. The voltage ripples of DPP output capacitor V_{C4} and switched capacitor V_{Csw4} are also shown.

air core inductor, used for both the transmitter side and the receiver side. The air core frame is 3D printed with an inner diameter of 20 mm and a length of 30 mm, and is wrapped by 23 turns of the AWG 46 Litz wire with #420 strands.

The design of the capacitive couplers is shown in Fig. 14. The landing/charging platforms are realized with two printed circuit boards (PCB). These two PCBs are put together to form the capacitive plates connected to the transmitter side. They contain a layer of copper, covered by a layer of solder mask for electric isolation. The rectangular UAV landing gears are made and utilized as capacitive plates for the receiver side. Polycarbonate sheets are used for this purpose, to provide the UAV with stiff but lightweight landing gears. These sheets are then wrapped with a layer of copper foil for conduction and an outer layer of Kapton® tape for insulation. This design procedure is demonstrated in the enlarged picture shown on the right side of Fig. 14. The dimensions of each landing gear are 450 mm \times 40 mm, whereas each PCB plate is $500 \text{ mm} \times 150 \text{ mm}$. The larger size of the PCB plates provides increased tolerance for misalignment of the landing gears. The capacitance between each PCB platform and UAV landing gear is approximately 800-1000 pF, yielding an equivalent total coupling capacitance of 400-500 pF. When the UAV is positioned on the charging platform, the minimal clearance between the landing gear and the landing platform ensures considerable coupling capacitance, thereby enhancing system efficiency and reducing the voltage stress across the plates. The proper operation of the power stage of DPP charging system does not rely on identifying whether a single UAV or multiple UAVs are being charged. In practical applications, wireless communication between UAVs and the landing platforms can be used to identify UAVs' charging requirements and activate the corresponding port.

Four different load configuration scenarios are tested:

• 1) interleaved four port operation: Four UAVs are charged at Ports #1, #3, #5 and #7, with an interleaved placement. The other ports are idle with no load, hence the cutoff switches

for these ports are turned off. This scenario of the load configuration is shown in Fig, 15 (a).

- 2) series four port operation: Four UAVs are charged at Ports #1, #2, #3 and #4, with a series placement. Other ports are idle with no load, hence the cutoff switches for these ports are turned off.
- 3) single port operation on Port #4: Only one UAV is present at Port #4, which sits in the middle of the series-stacked architecture. This scenario of the load configuration is shown in Fig, 15 (b).
- 4) single port operation on Port #8: Only one UAV is present at Port #8, which occupies the bottom of the series-stacked architecture.

Comparison tests between scenarios (1) and (2) are important to determine the optimal placement when multiple UAVs are present and charged. Comparison tests between scenarios (3) and (4) help to identify the optimal placement when a single UAV is present and charged. The full load condition with all eight ports active and driving maximum load is not tested because there is no power imbalance between each module. In this case, the series-stacked system achieves intrinsic voltage balancing without the DPP function and operates like eight independent CPT modules. Obtaining results for unbalanced load configurations (1)-(4) is more attractive. The experimental setup shown in Fig. 16 demonstrates the load configuration in scenario (1) (interleaved operation of four ports). The central hub of this setup is the main transmitter board, which hosts four UAVs on each side of the board. The receiver board and the adjustable resistive load are placed on top of the UAV, imitating real-world operating conditions. Litz-wires are used to interconnect all the boards, couplers, and loads. A single DC voltage source supplies the DPP converter with the 400 V high-voltage dc bus, resulting in a balanced 50 V on each DPP output capacitor. This balance is essential for achieving 50 V output voltage with unity gain on the UAV side, facilitated by the utilization of the CV operation mode in the CPT module and the design of the symmetrical compensation network. The oscilloscope displays the voltage and current waveforms of the CPT modules.

B. Experimental Results

Fig. 17 depicts the waveforms of the light load operation in scenario (2) (series operation of four ports). Fig. 17 (a) and (b) show the input voltages and currents of the CPT modules for Port #1, #2, #3 and #4. This configuration operates with a 400 V system input voltage, and the high levels of switched node voltages $V_{sw1}-V_{sw4}$ are at 50 V, representing the voltage balancing achieved by the DPP converter. All four ports are loaded with resistors set to identical values. Each port delivers an output power of approximately 25 W, resulting in a total output power of 100 W. This power balancing demonstrates the effectiveness of the compensation network design, as it enhances the tolerance of the system to variations in the coupling capacitance. Fig. 17 (c) shows the input and output switched-node voltages and currents of Port #1. The lagging of the input current to the input voltage helps the system achieve zero voltage switching (ZVS) and high efficiency.

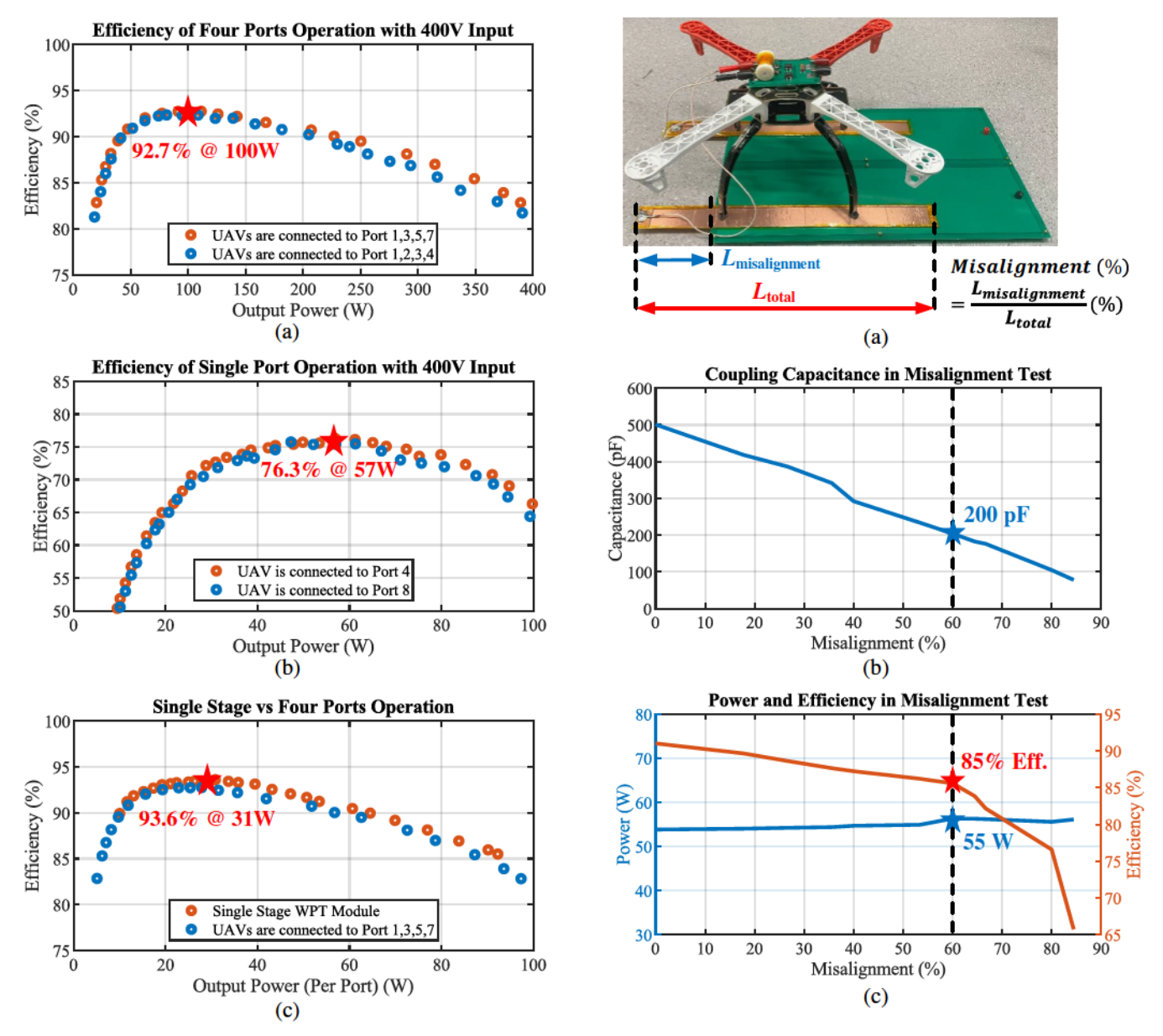


Fig. 20. Measured system efficiency under different load configurations: (a) efficiency comparison between two scenarios with interleaved and series four port operation; (b) efficiency comparison between two single port operations with Port #4 and Port #8 actively connected; (c) efficiency comparison between the interleaved four port operation and a single-stage CPT.

Fig. 21. UAV misalignment test for a single-stage CPT: (a) setup showing the definition of the misalignment percentage; (b) equivalent coupling capacitance versus the misalignment; (c) output power and CPT efficiency versus the misalignment.

Fig. 18 shows the waveforms of the full load operation in scenario (2) (series operation of four ports). Each port delivers approximately 100 W, resulting in 400 W total output power. Fig. 18 (a) and (b) show the input voltages and currents for Port #1, #2, #3 and #4 at a higher power level. 400 V bus voltage is set as the system input, and the high levels of the switched node voltages $V_{sw1}-V_{sw4}$ are still kept at 50 V, illustrating the effective voltage balancing mechanism of the DPP converter for wide operating conditions. Fig. 18 (c) shows the input and output switched-node voltages and currents of Port #1. Under the full load condition, the transmitter side loses ZVS under the full load operation because the input current leads the input voltage. Further analysis can be

conducted to calculate the current through each switch under various load configurations. With an accurate circuit modeling [23], [24], the parameters can be optimized to ensure ZVS across a wide range of operating conditions and minimize charge-sharing losses between switched capacitors, at the cost of increased circulating current and conduction losses

Fig. 19 shows the waveforms of light load operation in scenario (3) (single port operation on port #4). The switched node voltage V_{sw4} and input current I_{Lp4} are consistent with those in scenario (2), validating the independent operation of each port. The peak-to-peak voltage ripples of the DPP output capacitor V_{C4} and switched capacitor V_{Csw4} are within 0.5 V.

Fig. 20 shows the efficiency maps under different load operations. Fig. 20 (a) depicts the overall system efficiency

for scenarios (1) and (2). The efficiency of the interleaved configuration is 92.7% at 100 W output power and 82.8% at 390 W output power. The efficiency of the series configuration is 92.3% at 100 W output power and 81.7% at 390 W output power. The light load efficiency is similar for both cases while the efficiency is better for the interleaved configuration at heavier loads. Therefore, the interleaved configuration is more desirable for the operation of the DPP converter. Fig. 20 (b) shows the overall system efficiency for scenarios (3) and (4). The peak efficiency of the Port #4 connection is 76.3% at 57 W output power and the full load efficiency is 66.3% at 100 W. The peak efficiency of the Port #8 connection is 75.7% at 47 W output power and the full load efficiency is 64.4% at 100 W. The light load efficiency is also similar for both cases while the efficiency is higher for Port #4 connection at heavier loads since the DPP converter has lower loss when the load is connected in the middle of the series-stacked architecture instead of on the top or the bottom side. The efficiency of single port operation is much lower than that of four port operation, primarily due to higher hard switching loss and charge sharing loss. In four ports operation, the inductors in the compensation networks help more switched capacitors have soft charging and more switches have soft switching, which contributes to the overall efficiency improvement. Therefore, the proposed DWPT architecture is more attractive when multiple UAVs are being charged simultaneously. Fig. 20 (c) demonstrates the efficiency comparison between the interleaved four-port operation and a single-stage WPT. This single-stage WPT module consists solely of one CPT module, which operates with a 50 V input voltage and does not involve the DPP operation. The CPT module exhibits a peak efficiency of 93.6% at 31 W and maintains a full load efficiency of 85.5% at 92 W. The efficiency of the CPT module closely aligns with that of the four-port configuration, illustrating the minimal power loss and high efficiency of the DPP converter in stepping down a high input voltage of 400 V to multiple outputs of 50 V as CPT input voltages.

Fig. 21 (a) illustrates the misalignment test for a single-stage CPT module. The total length of the UAV landing gear is denoted as L_{total} while the length of the landing gear extending beyond the landing platform is represented as $L_{misalignment}$. This setup simulates the scenario where the landed UAV does not align perfectly with the landing platform. The misalignment percentage is defined as the ratio of $L_{misalignment}$ and L_{total} . Fig. 21 (b) demonstrates the relationship between the misalignment percentage and the equivalent coupling capacitance C_m . As misalignment increases, the capacitance decreases linearly, consistent with the theoretical equations for parallel plate capacitors. Fig. 21 (c) shows the output power and efficiency of the CPT module with a 35Ω load resistor. The output power remains stable at approximately 55 W, regardless of the misalignment, validating the effectiveness of the designed CV operational mode in maintaining consistent output power. The efficiency gradually decreases from 91% to 85% as misalignment increases from 0 to 60%. The system can maintain relatively high CPT efficiency over a wide range of misalignments. However, beyond 60% misalignment, the efficiency significantly drops due to the decreased equivalent coupling capacitance and greatly increased conduction loss.

VI. CONCLUSIONS

This paper presents the theoretical principles, design methods, and hardware implementation of a capacitive differential wireless power transfer architecture designed for a multi-UAV charging station. The DPP converter and the CPT modules are merged to reduce the component count and increase system efficiency. The capacitive coupler employs the landing platform and the UAV landing gears to achieve large coupling capacitance. The compensation network and the system resonant frequency are thoroughly analyzed and designed for a high misalignment tolerance and high efficiency. The practical concerns under no-load conditions are identified and addressed. An eight-port DPP converter is built and tested to drive multiple WPT ports with inherent voltage stepdown. The high system efficiency for the proposed DWPT architecture is validated through the experiments for multi-UAV charging from a high input voltage.

REFERENCES

- [1] M. Liao, T. Sen, Y. Elasser, H. Al Hassan, A. Pigney, E. Knapp, and M. Chen, "Drone charging stations on telecom towers with series-stacked capacitive differential wireless power transfer," *Proc. IEEE Appl. Power Electron. Conf. Expo.*, vol. 2, pp. 100–108, vol.2, 2024.
- [2] J. M. Arteaga, S. Aldhaher, G. Kkelis, C. Kwan, D. C. Yates, and P. D. Mitcheson, "Dynamic capabilities of multi-mhz inductive power transfer systems demonstrated with batteryless drones," *IEEE Transactions on Power Electronics*, vol. 34, no. 6, pp. 5093–5104, 2019.
- [3] P. K. Chittoor, B. Chokkalingam, and L. Mihet-Popa, "A review on UAV wireless charging: Fundamentals, applications, charging techniques and standards," *IEEE Access*, vol. 9, pp. 69 235–69 266, 2021.
- [4] C. Cai, X. Liu, S. Wu, X. Chen, W. Chai, and S. Yang, "A misalignment tolerance and lightweight wireless charging system via reconfigurable capacitive coupling for unmanned aerial vehicle applications," *IEEE Transactions on Power Electronics*, vol. 38, no. 1, pp. 22–26, January 2023.
- [5] F. Lu, H. Zhang, H. Hofmann, and C. C. Mi, "A double-sided LC-compensation circuit for loosely coupled capacitive power transfer," *IEEE Transactions on Power Electronics*, vol. 33, no. 2, pp. 1633–1643, 2018
- [6] S. Sinha, A. Kumar, B. Regensburger, and K. K. Afridi, "Design of high-efficiency matching networks for capacitive wireless power transfer systems," *IEEE Journal of Emerging and Selected Topics in Power Electronics*, vol. 10, no. 1, pp. 104–127, 2022.
- [7] F. Lu, H. Zhang, H. Hofmann, and C. C. Mi, "An inductive and capacitive combined wireless power transfer system with lc-compensated topology," *IEEE Transactions on Power Electronics*, vol. 31, no. 12, pp. 8471–8482, 2016.
- [8] Y. Zeng, C. Lu, R. Liu, X. He, C. Rong, and M. Liu, "Wireless power and data transfer system using multidirectional magnetic coupler for swarm auvs," *IEEE Transactions on Power Electronics*, vol. 38, no. 2, pp. 1440–1444, 2023.
- [9] Z. Yan, K. Zhang, L. Qiao, Y. Hu, and B. Song, "A multiload wireless power transfer system with concentrated magnetic field for auv cluster system," *IEEE Transactions on Industry Applications*, vol. 58, no. 1, pp. 1307–1314, 2022.
- [10] L. Tan, R. Zhong, Z. Tang, T. Huang, X. Huang, T. Meng, X. Zhai, C. Wang, Y. Xu, and Q. Yang, "Power stability optimization design of three-dimensional wireless power transmission system in multi-load application scenarios," *IEEE Access*, vol. 8, pp. 91 843–91 854, 2020.
- [11] P. S. Shenoy and P. T. Krein, "Differential power processing for dc systems," *IEEE Transactions on Power Electronics*, vol. 28, no. 4, pp. 1795–1806, 2013.
- [12] R. C. N. Pilawa-Podgurski and D. J. Perreault, "Submodule integrated distributed maximum power point tracking for solar photovoltaic applications," *IEEE Transactions on Power Electronics*, vol. 28, no. 6, pp. 2957–2967, 2013.

- [13] P. Wang, Y. Chen, J. Yuan, R. C. N. Pilawa-Podgurski, and M. Chen, "Differential power processing for ultra-efficient data storage," *IEEE Transactions on Power Electronics*, vol. 36, no. 4, pp. 4269–4286, 2021.
- [14] J. T. Stauth, M. D. Seeman, and K. Kesarwani, "Resonant switched-capacitor converters for sub-module distributed photovoltaic power management," *IEEE Transactions on Power Electronics*, vol. 28, no. 3, pp. 1189–1198, 2013.
- [15] K. A. Kim, P. S. Shenoy, and P. T. Krein, "Converter rating analysis for photovoltaic differential power processing systems," *IEEE Transactions* on *Power Electronics*, vol. 30, no. 4, pp. 1987–1997, 2015.
- [16] A. H. Chang, A.-T. Avestruz, and S. B. Leeb, "Capacitor-less photovoltaic (pv) cell-level power balancing using diffusion charge redistribution," in 2014 IEEE Applied Power Electronics Conference and Exposition - APEC 2014, 2014, pp. 712–720.
- [17] M. Liu, Y. Chen, Y. Elasser, and M. Chen, "Dual frequency hierarchical modular multilayer battery balancer architecture," *IEEE Transactions on Power Electronics*, vol. 36, no. 3, pp. 3099–3110, 2021.
- [18] A. M. Imtiaz and F. H. Khan, ""time shared flyback converter" based regenerative cell balancing technique for series connected li-ion battery strings," *IEEE Transactions on Power Electronics*, vol. 28, no. 12, pp. 5960–5975, 2013.
- [19] M. Evzelman, M. M. Ur Rehman, K. Hathaway, R. Zane, D. Costinett, and D. Maksimovic, "Active balancing system for electric vehicles with incorporated low-voltage bus," *IEEE Transactions on Power Electronics*, vol. 31, no. 11, pp. 7887–7895, 2016.
- [20] P. Wang, R. C. N. Pilawa-Podgurski, P. T. Krein, and M. Chen, "Stochastic power loss analysis of differential power processing," *IEEE Transactions on Power Electronics*, vol. 37, no. 1, pp. 81–99, 2022.
- [21] C. Pascual and P. Krein, "Switched capacitor system for automatic series battery equalization," in *Proceedings of APEC 97 - Applied Power Electronics Conference*, vol. 2, 1997, pp. 848–854 vol.2.
- [22] M. Liao, H. Li, P. Wang, T. Sen, Y. Chen, and M. Chen, "Machine learning methods for feedforward power flow control of multi-activebridge converters," *IEEE Transactions on Power Electronics*, vol. 38, no. 2, pp. 1692–1707, 2023.
- [23] M. Chen, K. K. Afridi, S. Chakraborty, and D. J. Perreault, "Multitrack power conversion architecture," *IEEE Transactions on Power Electron*ics, vol. 32, no. 1, pp. 325–340, 2017.
- [24] M. Chen, S. Chakraborty, and D. J. Perreault, "Multitrack power factor correction architecture," *IEEE Transactions on Power Electronics*, vol. 34, no. 3, pp. 2454–2466, 2019.
- [25] F. Lu, H. Zhang, H. Hofmann, and C. Mi, "A double-sided lclc-compensated capacitive power transfer system for electric vehicle charging," *IEEE Transactions on Power Electronics*, vol. 30, no. 11, pp. 6011–6014, 2015.



Tanuj Sen (Student Member, IEEE) received the bachelor's degree in Electrical and Electronics Engineering from Birla Institute of Technology and Science, Pilani, India in 2015 and his Master of Sciences degree in Electrical Engineering and Information Technology from ETH Zurich, Zurich, Switzerland in 2019, respectively. He received his M.A. degree in Electrical and Computer Engineering from Princeton University, NJ, USA in 2022. He is currently pursuing his Ph.D. degree in Electrical and Computer Engineering at Princeton University. His

research interests include the design of high-power density, high-frequency resonant power electronic inverters for powering plasma heating coils in fusion reactors, as well as the design and analysis of coupled inductors and their application in high-frequency power electronic circuits.



Youssef Elasser (Member, IEEE) received the B.S. degree in electrical engineering and computer science with a concentration in electric power from Rensselaer Polytechnic Institute, Troy, NY, USA, in 2018, and the M.A. and Ph.D. degrees in electrical engineering from Princeton University, Princeton, NJ, USA in 2020 and 2024, respectively. Since 2024, he has been with the Circuits Research Group, NVIDIA, Durham, NC, USA. His research interests include dc-dc power conversion, microprocessor voltage regulation and power delivery, and power

magnetics design and optimization. Dr. Elasser was the recipient of the Grainger Scholars Award for distinguished undergraduates studying electric power while at Rensselaer Polytechnic Institute (2018), two IEEE Transactions on Power Electronics Prize Paper Awards (2020, 2022), the first place award for IEEE Energy Conversion Congress and Exposition Student Demonstration (2021), and the prestigious National Science Foundation Graduate Research Fellowship while at Princeton University.



Mian Liao (Student Member, IEEE) received the B.S. degree in electrical engineering from Virginia Tech, VA, USA, in 2020, and the M.A. degree in electrical engineering in 2022 from Princeton University, NJ, USA, where he is currently working toward the Ph.D. degree. His research interests include machine learning control in power electronics, point-of-load converters for data center applications, wireless power transfer for UAV applications, and grid-tied three-phase inverters. Mr. Liao was the recipient of Fralin Undergraduate Research Fellowship

(2019) while at Virginia Tech, New Jersey Economic Development Authority Wind Institute Fellowship (2023) while at Princeton University, Rao R. Tummala Best Paper Award and First Prize Presentation Award at 3D-PEIM (2023), and the Best Presentation Award in the 2024 IEEE APEC.



Hashim A. Al Hassan (Member, IEEE) is currently the Director of Power Systems Analysis at UtilityInnovation Group where he leads power system modelling, analysis, system studies, and R&D for data centers and utility-scale microgrid systems. With over thirteen years of experience in the electric power industry, his roles spanned R&D, applications engineering, and product management. Specializing in power system modelling and solutions development, Dr. Al Hassan has developed numerous models for system analysis, informing innovative

solutions and product development in microgrids, medium voltage primary distribution systems, and transmission systems. He has authored or co-authored many peer-reviewed technical papers, and was awarded one patent. Dr. Al Hassan served as a reviewer for multiple IEEE journals and conferences. He held leadership roles in IEEE, including Topic Chair for the IEEE ECCE 2020 conference and Chair for the IEEE Power Electronics Society's Pittsburgh Chapter from 2021 to 2022. Dr. Al Hassan earned his B.S., M.S., and Ph.D. degrees in electrical engineering from the University of Pittsburgh in 2010, 2014, and 2018, respectively.



Andrew Pigney (Member, IEEE) is currently employed 15 years as Technology Principal at American Tower Corporation. Over 42 years of experience with the Wireless Communications Industry including Ericsson, Verizon and AT&T performing RF engineering, design and deployment for macro, small cell, DAS to C-RAN, vRAN and oRAN. Also skilled in RF antenna design and development, wireless infrastructure product engineering design and innovation for 4G, 5G and 6G technologies. U.S. Air Force (8 years) Electronic Warfare ECM,

COMINT surveillance on a variety of airborne platforms. University of the Air Force Avionics/ECM Systems Engineering Degree. Honorable Discharge from USAF in 1990.



Ed Knapp (Senior Member, IEEE) is American Tower's Chief Technology Officer. He is responsible for leading the company's global innovation program, technology investments and strategy for the wireless and data center platforms. Prior to joining American Tower in 2017, Mr. Knapp served as Senior Vice President of Engineering at Qualcomm. His research interests focused on 5G mmWave, small cells, CV2X and device to device communications. He joined Qualcomm after its acquisition of Flarion Technologies where his research and development

efforts served to enable OFDMA for 4G. Prior to that he served as the Chief Technology Officer of PacketVideo Corporation where he worked on the initial MPEG streaming services over cellular networks. He co-founded NextWave Telecom, Inc. in 1995 and served as its Chief Technology Officer, and was Executive Director of Technical Services for Bell Atlantic/NYNEX Mobile (Verizon Wireless).

Mr. Knapp serves on the Board of Directors of AST SpaceMobile and the Center for Automotive Research. He is a member of the CEAS Dean's Advisory Council at Stony Brook University as well as the Rutgers University Industry Advisory Board. Mr. Knapp currently has five granted U.S. patents and one pending application. He earned an M.B.A. from Columbia University, a Master of Science in Electrical Engineering from Polytechnic University (NYU) in New York and a Bachelor of Science in Engineering from Stony Brook University.



Minjie Chen (Senior Member, IEEE) received the S.M., E.E., and Ph.D. degrees in electrical engineering and computer science from Massachusetts Institute of Technology, Cambridge, MA, USA, in 2015 and the B.S. degree in electrical engineering from Tsinghua University, Beijing, China, in 2009. He is an Associate Professor of Electrical and Computer Engineering and the Andlinger Center for Energy and the Environment at Princeton University. His research interests include modeling, design, and application of high-performance power electronics.

Dr. Chen is the recipient of the IEEE PELS Richard M. Bass Outstanding Young Power Electronics Engineer Award, the Princeton SEAS E. Lawrence Keyes, Jr./Emerson Electric Co. Junior Faculty Award, the NSF CAREER Award, seven IEEE Transactions on Power Electronics Prize Paper Awards, the C3.ai Faculty Award, the Princeton Innovation Award, the ASAE Power of Associations Silver Award, the MIT EECS D. N. Chorafas Ph.D. Thesis Award, and numerous conference Best Paper Awards from COMPEL, ICRA, IROS, ECCE, APEC, 3D-PEIM, and OCP. He was listed on the Princeton Engineering Commendation List for Outstanding Teaching multiple times. He is an Associate Editor of the IEEE Transactions on Power Electronics and the IEEE Journal of Emerging and Selected Topics in Power Electronics. He is an IEEE PELS Distinguished Lecturer, the vice chair of IEEE PELS TC10-Design Methodologies, and has launched the IEEE PELS MagNet Challenge.